

An Energy-Efficient RFET-Based Stochastic Computing Neural Network Accelerator

Sheng Lu, *Student Member, IEEE*, Qianhou Qu, *Student Member, IEEE*, Sungyong Jung, *Member, IEEE*,
Qilian Liang, *Fellow, IEEE*, and Chenyun Pan, *Senior Member, IEEE*

Abstract—Stochastic computing (SC) offers significant reductions in hardware complexity for traditional convolutional neural networks (CNNs). However, despite its advantages, stochastic computing neural networks (SCNNs) often suffer from high resource consumption due to components such as stochastic number generators (SNGs) and accumulative parallel counters (APCs), which limit overall performance. This paper proposes a novel SCNN architecture leveraging reconfigurable field-effect transistors (RFETs). The inherent reconfigurability at the device level enables the design of highly efficient and compact SNGs, APCs, and other related essential components. Furthermore, a dedicated SCNN accelerator architecture is developed to facilitate system-level simulation. Based on accessible open-source standard cell libraries, experimental results demonstrate that the proposed RFET-based SCNN accelerator achieves significant reductions in area, latency, and energy consumption compared to its FinFET-based counterpart at the same technology node.

Index Terms—Reconfigurable field-effect transistors, stochastic computing, stochastic number generator, accumulative parallel counter, convolutional neural network, approximate computing.

I. INTRODUCTION

WITH the advancement of neural network technologies, various alternative computing paradigms have been proposed to address the growing demand for efficient hardware implementations [1, 2]. Among these approaches, the stochastic computing neural network (SCNN) emerges as a promising solution due to its fundamental differences from conventional binary computing [3-6]. SCNN enables low-cost hardware implementations, offering high power efficiency and inherent fault tolerance. It significantly reduces the hardware complexity of fundamental arithmetic units, such as adders and multipliers, which typically occupy a substantial portion of the system's overall computing resources.

SCNNs typically require a large number of stochastic number generators (SNGs) [7, 8], each consisting of a random number source (RNS) and a probability conversion circuit

This work is funded by the Advanced Scientific Computing Research (ASCR) program of the Department of Energy (DOE) through award DE-SC0022881, and National Science Foundation (NSF) under grant CCF-2219753.

S. Lu, Q. Qu, Q. Liang, and C. Pan are with the Department of Electrical Engineering, The University of Texas at Arlington, Arlington, TX 76010, USA. (email: sxl2408@mavs.uta.edu)

S. Jung is with the Department of Electrical Engineering and Computer Science, South Dakota State University, Brookings, SD 57007, USA.

(PCC) to convert binary-encoded values into stochastic bitstreams. SNGs can occupy up to 90% of the total system area, as reported in previous studies [9-11]. To mitigate this overhead, various optimization techniques have been proposed. For the RNS component, one of the most effective methods is RNS sharing, which reduces area and cost by distributing the output bitstreams of linear feedback shift registers (LFSRs) across multiple SNGs via signal shuffling. In contrast, optimizing the PCC is more challenging. The traditional comparator-based (CMP) PCC, while simple, incurs high area overhead. To address this, alternative designs such as the weighted binary generator (WBG) and the multiplexer chain (MUX-chain) are proposed [8]. Although the MUX-chain offers the best improved hardware efficiency, the PCC still dominates both the area and energy consumption.

Besides SNGs, another key component in stochastic computing is the accumulative parallel counter (APC), which is widely used in the stochastic domain. Unlike the adders employed in conventional digital neural networks, the APC is used to accumulate multiplication results produced by stochastic multipliers while converting stochastic bitstreams into binary values, thereby serving as a bridge between the stochastic and binary domains. An APC typically consists of full adders (FAs) and half adders (HAs) arranged in a carry-propagation-like topology. Although this structure provides high accuracy and a straightforward implementation, it usually incurs a relatively large area overhead. To address this issue, the approximate accumulative parallel counter (AxPC) is proposed [12]. In AxPC designs, simple logic gates are used in the first stage to perform parity (odd–even) checking instead of exact addition, which reduces hardware complexity at the cost of reduced computational accuracy.

In addition to circuit-level optimization, beyond-CMOS technologies exhibit significant potential in addressing the challenge [13-16]. Among emerging device technologies, the reconfigurable field-effect transistor (RFET) is particularly well-suited for this application. Owing to its inherent device-level ambipolarity—enabling dynamic switching between p-type and n-type operations [17-20], RFETs are well-suited for implementing various digital logic components, including full adders (FAs) [21-23], look-up tables (LUTs) [24], multiplexers [25], and so on. Existing studies have explored the design of key neural network components based on RFETs, such as approximate compressors and multipliers [16, 26]. However, these works primarily focus on optimizing traditional digital

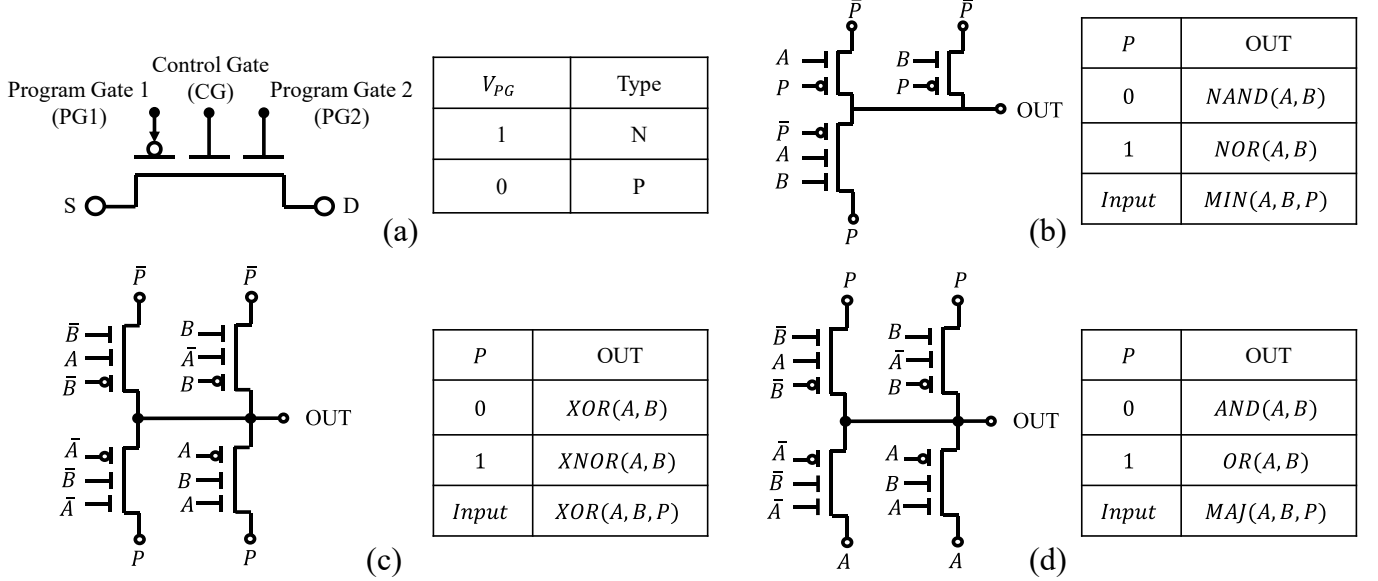


Fig. 1. (a) Symbol of an RFET device includes program gates, allowing it to be switched between n- and p-type operations by applying different gate voltages to the program gates. (b) – (d) Reconfigurable logic gates based on RFETs.

neural networks and circuits rather than SCNNs. For the SNG, we demonstrate that an RFET NAND–NOR chain-based PCC achieves significant improvements in area, delay, and energy efficiency while maintaining accuracy. For the APC part, two AxPC architectures based on RFET high-efficiency FAs and compressors are proposed. The first design employs RFET 3-input majority gates as the input layer to further reduce area, delay, and energy at the cost of a slight loss in accuracy, whereas the second design is based on an RFET 4:2 compressor input layer, which significantly improves accuracy while preserving the performance advantage.

In this work, an RFET-based SCNN architecture is proposed, demonstrating notable performance improvements over FinFET-based counterparts at the same technology node. Two primary functional units are investigated: the RFET-based PCC and the RFET-based AxPC. The key contributions of this paper are outlined as follows:

- We design a novel PCC structure based on RFET reconfigurable NAND-NOR gates with theoretical analysis, achieving reduced area, delay, and energy consumption compared to its FinFET-based counterpart.
- We propose two RFET-based AxPC architectures based on high-efficiency RFET logic units, which can be applied in different scenarios and offer flexibility in accuracy and hardware efficiency trade-offs.
- We present an SCNN system architecture and perform a fair system-level comparison between RFET-based and FinFET-based implementations.
- We propose a pipelining strategy between memory access and computational resource balance to improve overall system efficiency.

II. BACKGROUND

A. RFET Basic

RFETs are characterized by multiple gate terminals, including two program gates (PGs) that control the polarity of the transistor, and a control gate (CG) that regulates its switching behavior [17, 20]. **Fig. 1(a)** illustrates the symbol of a tri-gate RFET along with its ambipolarity working principle. The RFET operates in the ON state only when all program gates and the control gate are biased at an identical voltage level. A defining property of the RFET is that its on-state resistance is predominantly governed by the barrier resistance at the source side, while the addition of multiple gate terminals exerts only a marginal influence on the drive current [27, 28]. Moreover, RFETs exhibit extremely low leakage currents [29], making them highly attractive for energy-efficient electronic systems [20]. According to recent fabrication studies, RFETs are compatible with standard CMOS process technologies, facilitating seamless integration into current nanoscale CMOS manufacturing processes without substantial changes to materials or processing steps [30, 31]. Nonetheless, limitations such as relatively lower drive current in the ON state and a comparatively larger device footprint may hinder RFETs from fully replacing conventional CMOS transistors in all applications.

A direct benefit of this ambipolarity is the ability to design multi-functional logic gates. For example, as shown in **Fig. 1(b)**, a three-transistor gate can switch between NAND and NOR logic functions based on the applied programming voltage. When utilizing the program pin as the third input, RFET can build compact reconfigurable three-input logic gates, such as MIN3, XOR3 and MAJ3, as shown in **Fig. 1(b), (c)** and

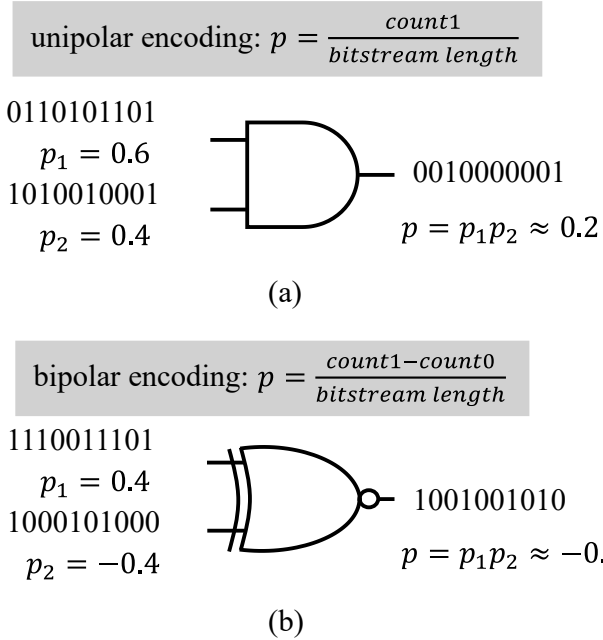


Fig. 2. Multiplication based on stochastic computing [4]. (a) Unipolar encoding with AND gate, and (b) bipolar encoding with XNOR gate.

(d). This device-level reconfigurability enables more efficient and compact circuit designs, making RFETs particularly well-suited for area- and power-constrained applications.

B. Stochastic Computing Basic

Unlike conventional binary computation, stochastic computing performs arithmetic operations using sequential bitstreams, where the number of ‘1’s and ‘0’s—corresponding to high and low voltage levels—encodes numerical values. Two primary encoding schemes are commonly employed: unipolar encoding, which represents values in the range [0, 1], and bipolar encoding, which represents values in the range [-1, 1] [3]. The fundamental concepts of both encoding schemes are illustrated in **Fig. 2**. For instance, to represent the value 0.4 in unipolar encoding, a bitstream containing 40% randomly distributed ‘1’s suffices.

Due to the nature of stochastic representation, the corresponding arithmetic circuits in SC differ significantly from those used in traditional binary logic. As shown in **Fig. 2**, multiplication can be implemented using a simple AND gate in the unipolar domain or an XNOR gate in the bipolar domain. Similarly, addition can be realized using lightweight logic elements, such as OR gates or MUXes, enabling highly area- and energy-efficient circuit designs [4]. Furthermore, by appropriately combining or utilizing certain logic gates, more complex computations—such as proportional scaling and approximation of unary linear functions—can be achieved [32], thereby offering greater potential for implementing neural network-related operations.

C. Stochastic Computing Neuron Structure

Although numerous convolutional neural network (CNN)

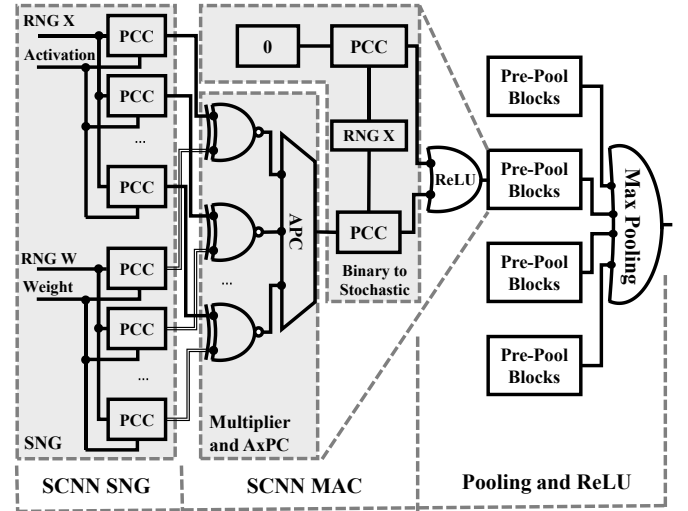


Fig. 3. Stochastic neuron proposed by Frasser et al. with fully correlated inputs to both ReLU and MP components to reduce hardware area [35].

architectures exist, the fundamental building block of these models is the neuron. A CNN neuron is a computational unit characterized by local receptive fields, shared weights, and a nonlinear activation function, enabling the extraction of local features from input images or data [33]. At the hardware level, a neuron may be implemented using multipliers and adders to perform convolutional or multiplicative operations [34]. Activation functions, such as Rectified Linear Unit (ReLU) or Sigmoid, can be realized through corresponding dedicated logic circuits. Furthermore, pooling operations, commonly employed in CNNs, serve as downsampling mechanisms that reduce the spatial dimensions of feature maps while retaining essential information.

The basic neuron structure in SCNNs follows a similar architecture, as shown in **Fig. 3**. This design, proposed by Frasser et al., presents an SC neuron that leverages input correlation to reduce hardware area costs [35]. The neuron employs two RNGs in total. One RNG is used to encode the activation values and to generate correlated input streams for the ReLU and Max Pooling (MP) operations. The other RNG is used to encode the weights. As previously discussed, in stochastic computing, an OR gate can function as an adder when the input bitstreams are statistically independent. However, when the bitstreams are fully correlated—such as when generated from the same RNG—the OR gate tends to behave more like a maximum operator. This behavior can be exploited to implement ReLU and MP functions efficiently. In contrast to traditional digital neurons, which typically employ adder tree structures to accumulate the outputs from multiple multipliers, SC neurons utilize an APC to perform the summation. The APC operates on the input bits at each clock cycle and outputs the count of logic ‘1’s in binary format. Following this, a binary-to-stochastic (B2S) converter is used to transform the binary sum back into stochastic format, enabling continued processing within the SC domain.

The neuron structure shown in **Fig. 3** not only reduces the

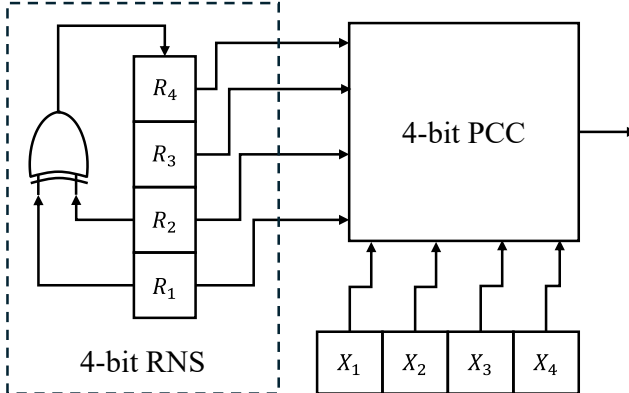


Fig. 4. Example circuit schematic of a 4-bit SNG [11].

hardware area required for addition and multiplication but also simplifies the implementation of activation and pooling functions, which typically demand significantly more area in conventional digital neuron designs. Due to these advantages, this structure is adopted as the fundamental building block of the proposed SCNN architecture.

D. Stochastic Number Generator

The SNG consists of two main components: an RNS and a PCC. The most used RNS is the LFSR, which generates pseudo-random sequences by shifting bits through a register and applying a linear function—typically an XOR—on selected bits to determine the new input bit. An LFSR can produce a maximum-length pseudo-random sequence of $2^n - 1$ distinct states for an n -bit register when its feedback polynomial is primitive, ensuring that it cycles through all possible non-zero states before repeating. As illustrated in **Fig. 4**, which shows an example of a 4-bit SNG, the left side consists of a 4-bit LFSR, while the right side features a 4-bit PCC [11]. The PCC generates one stochastic bit per clock cycle based on the binary value from the LFSR and the given input.

Fig. 5 presents two typical implementations of the PCC [10, 11]. **Fig. 5(a)** shows the traditional comparator design, which compares the input binary number with the random number generated by the random number source cycle by cycle. If the input number X is greater than the random number R , the output is logic ‘1’; otherwise, the output is logic ‘0’. **Fig. 5(b)** illustrates the MUX-chain-based PCC. Unlike the comparator-based design, the MUX-chain PCC does not perform a direct comparison between the input and the random number. Instead, it operates probabilistically by selecting signals through a chain of multiplexers. Assuming that the random bits are independent, the output probability depends on the configuration of the MUX-chain and the input value. The output probability can be expressed as [10]:

$$P = \frac{\sum_{i=0}^{N-1} X_i 2^i}{2^N} \quad (1)$$

Based on this expression, the MUX-chain PCC effectively transforms the input binary number into a probability value between 0 and 1, depending on the value of the input. With a

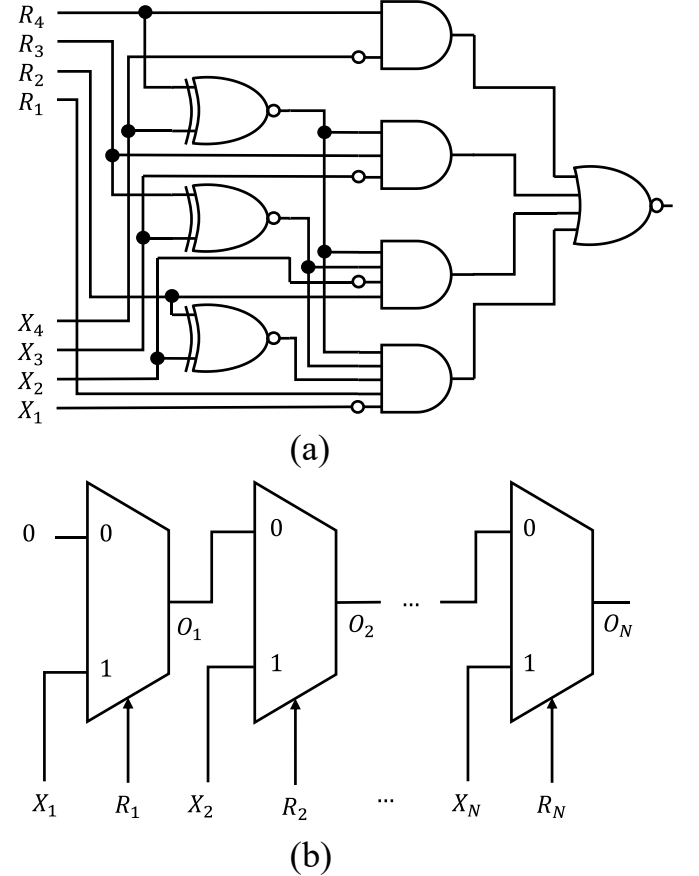


Fig. 5. Commonly used PCCs. (a) CMP-based 4-bit PCC [11], and (b) MUX-chain-based N-bit PCC [10].

sufficiently long bitstream, the output closely approximates the corresponding real-valued representation of the input.

A key advantage of the MUX-chain-based PCC is its significant reduction in hardware area. Compared to the comparator-based design, it can achieve area savings of up to 43% and 58% in 4-bit and 8-bit configurations [11], respectively. Thanks to its efficient and compact nature, it has been adopted for certain chip tape-out works [36]. However, this benefit comes with a trade-off, as the increased length of the multiplexer chain may lead to higher propagation delay within the PCC.

III. PROPOSED RFET-BASED STOCHASTIC COMPUTING

A. RFET-based Probability Conversion Circuit

As shown in **Fig. 5(b)**, an i -stage MUX21 logic gate in the MUX-chain has the following logic expression:

$$MUX(O_{i-1}, X_i, R_i) = O_{i-1} \cap \overline{R_i} \cup X_i \cap R_i, (i > 1) \quad (2)$$

which can be further decomposed into an equivalent logic expression [10], as shown in **Fig. 6(a)**:

$$\begin{cases} MUX(O_{i-1}, R_i) = O_{i-1} \cap \overline{R_i}, & X_i \equiv 0 \\ MUX(O_{i-1}, R_i) = O_{i-1} \cup R_i, & X_i \equiv 1 \end{cases} \quad (3)$$

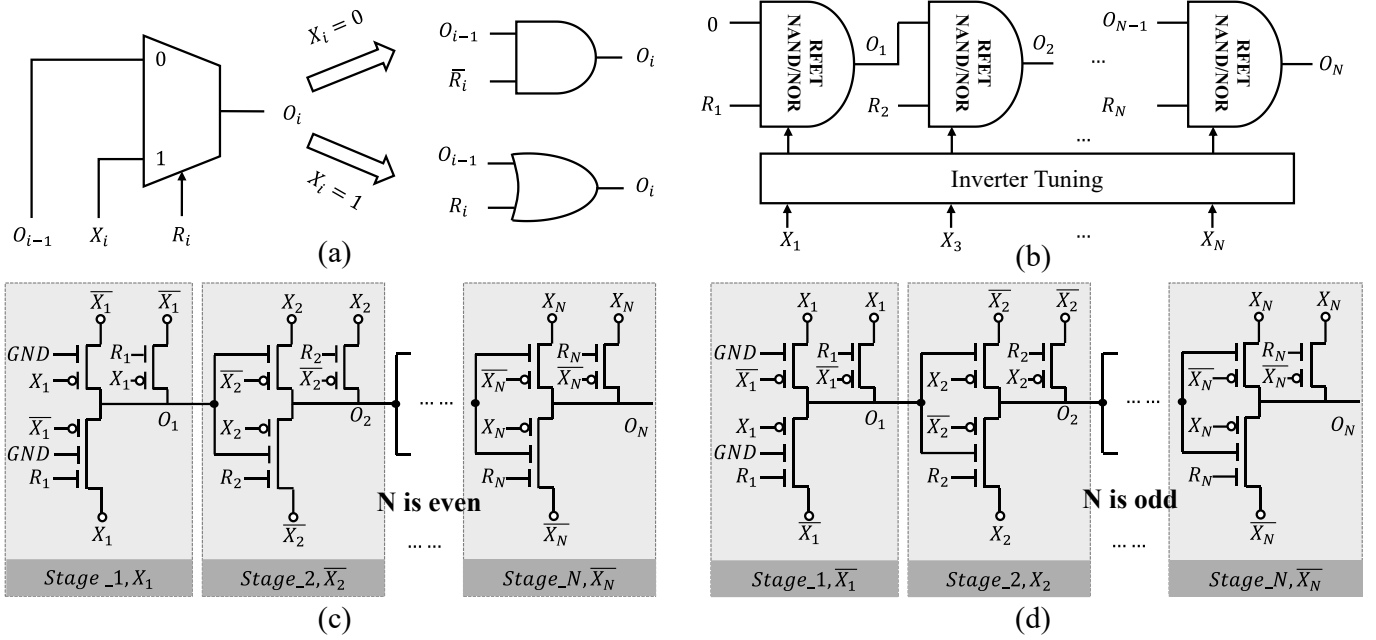


Fig. 6. (a) Equivalent representation of MUX21 using AND/OR gates. (b) RFET-based NAND-NOR PCC with tuned inverters. (c) Detailed circuit of NAND-NOR PCC with even input number. (d) Detailed circuit of NAND-NOR PCC with odd input number.

This operating principle closely resembles that of a reconfigurable logic gate if the \$X_i\$ is the programming signal and \$O_{i-1}\$ and \$R_i\$ are inputs [21]. The problem is that, though expression (3) is close to the NAND-NOR reconfigurable logic gate, multiple inverters are needed to make the NAND-NOR PCC work in the same way. Another 2 inverters are needed, the first one is put after the final output, and another is put before the \$R_i\$. Although the RFET-based NAND-NOR gate requires fewer transistors compared to a CMOS-based MUX gate, the advantage diminishes when additional inverters are included. Considering the larger footprint of a single RFET device, the overall area may show no improvement—or even result in overhead—in RFET-based PCC designs. To address this issue, we tune the input signal by intermittently inserting inverters along the \$X_i\$ input port, as shown in Fig. 6(c) and (d).

Lemma 1

Let \$X_1, X_2, \dots, X_N\$ be the independent Bernoulli random variables with \$P(X_i = 1) = p_i\$, and let \$R_1, R_2, \dots, R_N\$ be the independent Bernoulli random variables with \$P(R_i = 1) = 0.5\$, independent of all \$X_i\$. Define the cascaded outputs recursively as:

$$O_1 = NAND(0, R_1) \cap \bar{X}_1 + NOR(0, R_1) \cap X_1 \quad (4)$$

And for \$i \geq 2\$, if total chain length **N is even**

$$O_i = \begin{cases} NAND(O_{i-1}, R_i) \bar{X}_i + NOR(O_{i-1}, R_i) X_i, & i \text{ odd} \\ NAND(O_{i-1}, R_i) X_i + NOR(O_{i-1}, R_i) \bar{X}_i, & i \text{ even} \end{cases} \quad (5)$$

If total chain length **N is odd**,

$$O_i = \begin{cases} NAND(O_{i-1}, R_i) X_i + NOR(O_{i-1}, R_i) \bar{X}_i, & i \text{ odd} \\ NAND(O_{i-1}, R_i) \bar{X}_i + NOR(O_{i-1}, R_i) X_i, & i \text{ even} \end{cases} \quad (6)$$

Equations (5) and (6) indicate that when the following inverter adding rule is satisfied:

If N is even, add inverters to all \$X_i\$ with even index

If N is odd, add inverters to all \$X_i\$ with odd index

NAND-NOR chain can realize the same function as the MUX-chain structure.

Proof:

Stage 1 Expectation

Since \$NAND(0, R_1) = 1\$ and \$NOR(0, R_1) = \bar{R}_1\$,

$$O_1 = \begin{cases} 1, X_1 = 0 \\ \bar{R}_1, X_1 = 1 \end{cases} \quad (7)$$

Therefore, the expected value is

$$m_1 = \mathbb{E}(O_1) = 1 - \frac{1}{2}X_1 \quad (8)$$

General Stage Recurrence, assuming **N is even**

For \$i \geq 2\$, conditional expectations yield:

- If stage i selects NAND, then

$$\mathbb{E}[O_i | O_{i-1}] = 1 - \frac{1}{2}m_{i-1} \quad (9)$$

- If stage i selects NOR, then

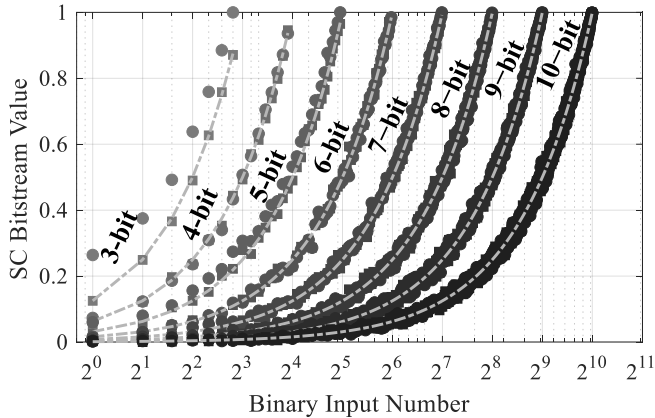


Fig. 7. Conversion results of binary numbers with varying bit lengths under different PCC precisions. Circles denote RFET NAND-NOR PCC, squares denote MUX-chain PCC, and the dashed line indicates CMP-PCC. Curves from left to right are 3-bit to 10-bit PCCs.

$$\mathbb{E}[O_i | O_{i-1}] = \frac{1}{2} - \frac{1}{2}m_{i-1} \quad (10)$$

Introduce indicator s_i for NAND-NOR selection:

$$s_i = \begin{cases} X_i, & i \text{ is even} \\ 1 - X_i, & i \text{ is odd} \end{cases} \quad (11)$$

Taking expectations over O_{i-1} , the recurrence for the values is:

$$m_i = \mathbb{E}[s_i \text{NAND}(O_{i-1}, R_i) + (1 - s_i) \text{NOR}(O_{i-1}, R_i)] \quad (12)$$

$$m_i = -\frac{1}{2}m_{i-1} + c_i \quad (13)$$

where

$$c_i = \frac{1}{2}(1 + s_i) \in \left\{ \frac{1}{2}, 1 \right\} \quad (14)$$

Unfolding the recurrence, for any $N \geq 2$,

$$m_i = \left(-\frac{1}{2} \right)^{N-1} m_1 + \sum_{k=2}^N \left(-\frac{1}{2} \right)^{N-k} c_k \quad (15)$$

Unrolling the recurrence

Substitute $m_1 = 1 - \frac{1}{2}X_1$ and $c_k = \frac{1}{2}(1 + s_k)$:

$$m_N = \left(-\frac{1}{2} \right)^{N-1} \left(1 - \frac{1}{2}X_1 \right) + \frac{1}{2} \sum_{k=2}^N \left(-\frac{1}{2} \right)^{N-k} + \frac{1}{2} \sum_{k=2}^N \left(-\frac{1}{2} \right)^{N-k} s_k \quad (16)$$

Substitute s_k in terms of X_k :

$$\sum_{k=2}^N \left(-\frac{1}{2} \right)^{N-k} s_k = \sum_{k=2, \text{even}}^N \left(-\frac{1}{2} \right)^{N-k} X_k + \sum_{k=3, \text{odd}}^N \left(-\frac{1}{2} \right)^{N-k} (1 - X_k) \quad (17)$$

Use constant terms and coefficients instead,

$$m_N = A_N + \sum_{k=1}^N \alpha_k X_k \quad (18)$$

where

$$A_N = \left(-\frac{1}{2} \right)^{N-1} + \frac{1}{2} \sum_{k=2}^N \left(-\frac{1}{2} \right)^{N-k} + \frac{1}{2} \sum_{k=3, \text{odd}}^{N-1} \left(-\frac{1}{2} \right)^{N-k} \quad (19)$$

$$\alpha_k = \frac{2^{k-1}}{2^N} \quad (20)$$

Simplified expression

$$m_N \approx \sum_{k=1}^N \frac{2^{k-1} X_k}{2^N} \quad (21)$$

Same way, we can get the m_N under **N is odd**,

$$m_N \approx \sum_{k=1}^N \frac{2^{k-1} X_k}{2^N} \quad (22)$$

Based on equations (21) and (22), we prove that the final output of the RFET NAND-NOR-chain is positively correlated with the value of the input binary number X , which enables the conversion of the binary number into a decimal value between 0 and 1 with unipolar encoding. **Fig. 7** illustrates the conversion results of binary numbers to unipolar encoding SC bitstream with different bit lengths under different size PCC conditions. The circles represent the RFET NAND-NOR PCC, the squares represent the MUX-chain PCC, and the dashed line in the middle represents the CMP-PCC. It can be observed that when handling smaller bit lengths, the NAND-NOR PCC results in a slightly higher value compared to the other two methods. This is because in equation (18), there is a constant term before the summation operator.

B. RFET-based Approximate Accumulative Parallel Counter

APC is widely used in stochastic computing to transform stochastic signals into binary signals. Using **Fig. 8(a)** as an example [12], during each clock cycle, the APC samples the 25 input signals and counts the number of logic ‘1’s present. The counting operation is implemented using a hierarchical adder tree composed of half adders and full adders, which generate partial sums and carry bits in parallel. These partial results are successively combined across multiple stages to accumulate the total count. The final output is a 5-bit binary number representing the total number of logic ‘1’s among the inputs, with the maximum count of 25.

Although the APC can count the number of logic ‘1’s in parallel without error, it consumes a large number of adders, especially when the number of inputs is high. To address this issue, the approximate accumulative parallel counter (AxPC) has been proposed [12]. In AxPC, simple logic gates are employed in the first stage to realize parity (odd–even) checking functions instead of exact addition. For example, in the referenced work [16], the first-layer full adders are replaced with NAND and NOR gates, which significantly reduces the circuit area. However, the area savings achieved by AxPC come at the cost of reduced counting accuracy.

In this work, we propose implementing and optimizing the AxPC design with RFET technology. **Fig. 8(b)** demonstrates

ENERGY-EFFICIENT RFET-BASED STOCHASTIC COMPUTING NN ACCELERATOR

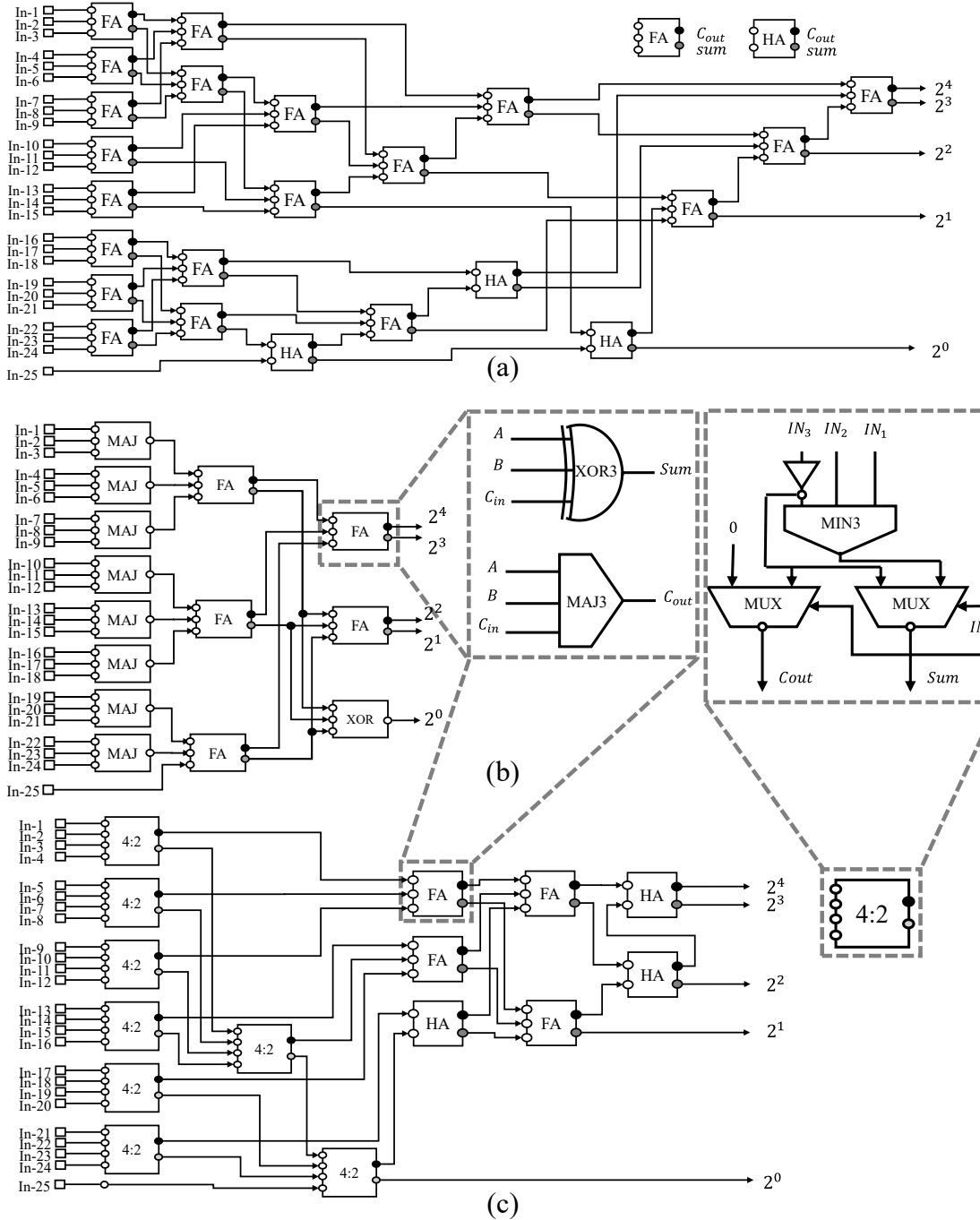


Fig. 8. (a) Traditional APC structure with 25 inputs. (b) Proposed RFET-based compact MAJ-AxPC structure. (c) Proposed RFET-based high accuracy COMP-AxPC structure.

the usage of RFET technology to build compact 25-input MAJ-AxPC. The RFET-based FA only needs two reconfigurable gates—XOR3 and MAJ3, along with a few inverters, are required. In the first stage, MAJ3 gates are used to generate the carry information, while the parity information is discarded. This structure achieves ultra-high area efficiency while maintaining considerable accuracy, as will be demonstrated in the following discussion. The architecture is particularly suitable for RFET technology because, compared with a conventional CMOS-based full adder that typically requires up

to 28 transistors, the RFET-based solution achieves significant reductions in transistor count and circuit area, even when considering the larger footprint of individual RFET devices, thereby reducing energy consumption.

Moreover, since both the referenced AxPC and the proposed MAJ-AxPC achieve area savings by sacrificing system accuracy, we propose an RFET-based 4:2 compressor AxPC (COMP-AxPC) that significantly improves accuracy while still maintaining area reduction compared with the traditional APC design. As shown in **Fig. 8(c)**, the first layer of

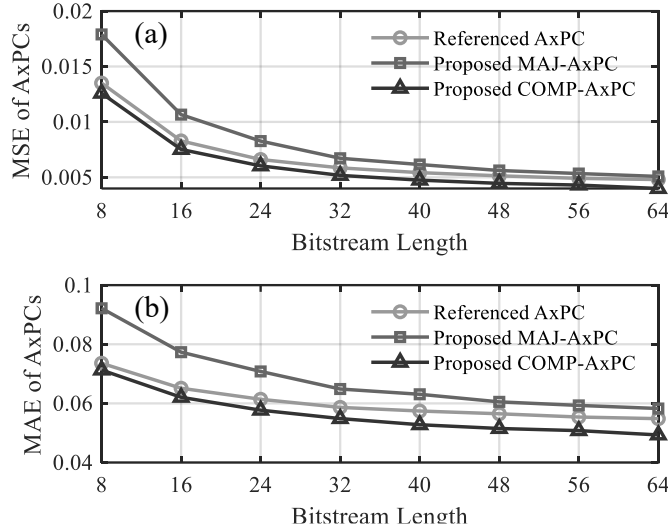


Fig. 9. (a) Relationship between MSE and bitstream length for the reference AxPC and the proposed MAJ- and COMP-AxPC unit. (b) Relationship between MAE and bitstream length for the reference AxPC and the proposed MAJ- and COMP-AxPC unit. The baseline corresponds to the exact APC.

full adders is replaced by RFET-based compact 4:2 compressors [16], which will enhance the circuit's accuracy and keep the area efficient.

Fig. 9 shows the mean squared error (MSE) and mean absolute error (MAE) as functions of the bitstream length for the referenced AxPC and proposed AxPCs, with the exact APC used as the baseline. The results are obtained from Monte Carlo simulations in which stochastic bitstreams are generated for 25 inputs, and the counter outputs are converted into stochastic outputs by a 5-bit B2S unit. For each Monte Carlo run, the output of each counter is averaged over the bitstream length. Let y_{APC}^i and y_{AxPC}^i denote the averaged outputs of the exact APC and an approximate APC, respectively, in the i -th run, and let N be the total number of runs. The MSE and MAE are defined as

$$MSE = \frac{1}{N} \sum_{i=1}^N (y_{AxPC}^i - y_{APC}^i)^2 \quad (23)$$

$$MAE = \frac{1}{N} \sum_{i=1}^N |y_{AxPC}^i - y_{APC}^i| \quad (24)$$

The proposed MAJ-AxPC is primarily designed to achieve ultra-high area efficiency, which results in a slight sacrifice in counting accuracy. Although the proposed MAJ-AxPC exhibits slightly higher error than the traditional AxPC at shorter bitstream lengths, the error gap between the traditional AxPC and the proposed MAJ-AxPC steadily decreases as the bitstream length increases. This trend indicates that the accuracy loss introduced to improve area efficiency becomes negligible for longer bitstreams, making the proposed MAJ-AxPC sufficiently accurate and well suited for practical

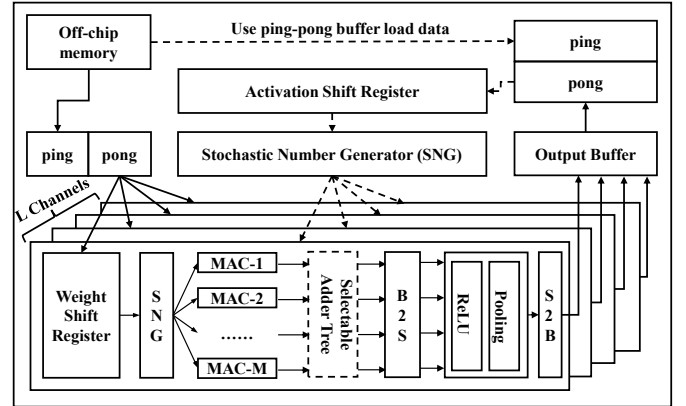


Fig. 10. Overall SC accelerator architecture [37].

applications. In contrast, the proposed COMP-AxPC achieves the highest accuracy among all AxPC designs, with its MSE and MAE reduced to 12.7% and 7.5%, respectively, of those of the referenced AxPC. The hardware cost and detailed parameter comparisons are presented in the next section. In this work, we adopt the COMP-AxPC as the final solution due to its high accuracy and area efficiency when implemented using RFET technology.

IV. SCNN ACCELERATOR ARCHITECTURE

A. Architecture Modeling Description

The proposed architecture, shown in **Fig. 10** [37], integrates a ping-pong buffering mechanism with activation and weight shift registers to ensure efficient data transfer from off-chip memory. In each channel, an SNG converts both activations and weights into stochastic bit streams, which are processed by 16 parallel multiply-accumulate (MAC) units to exploit parallelism. Each MAC unit comprises 25 parallel multipliers and a 25-input COMP-AxPC, followed by a configurable adder tree designed to support neurons with many inputs in fully connected layers. For convolutional layers, the adder tree can be bypassed. Subsequently, a B2S converter is employed to enable transformations and preserve compatibility within the stochastic domain. After computation, the results pass through an optional ReLU/ MP stage and a stochastic to binary (S2B) converter that converts outputs back to binary representation [38]. The final results are stored in the output buffer.

This architecture can be modified for different channel numbers, making it adaptable to various application scenarios. The system is based on 8-bit accuracy, with weights and activations loaded from off-chip GDDR5 memory operating at 7000 MHz, providing a loading speed of approximately 224 B/ns.

B. Pipeline Strategy for Off-Chip Memory Bandwidth Limit

Based on the proposed architecture, an important optimization problem arises: how to efficiently utilize the available logic resources under the constraint of limited off-chip data loading bandwidth. The proposed strategy is to

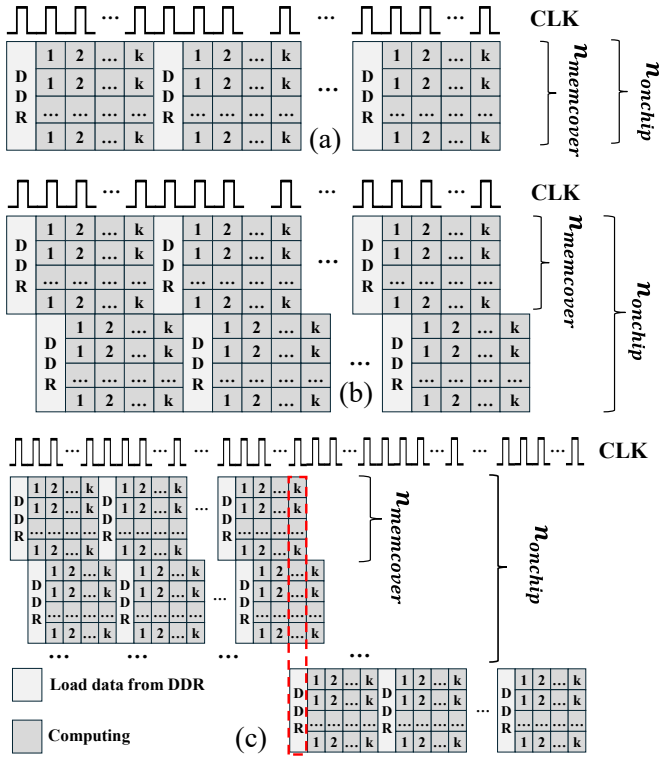


Fig. 11. Proposed pipeline strategy under different application scenarios: (a) no pipeline, (b) partial pipeline, and (c) full pipeline.

implement pipelining across different bits within the bitstream to maximize the utilization of data loaded from off-chip memory.

Three pipeline strategies are proposed: no pipeline, partial pipeline, and full pipeline. In the no-pipeline case, when the data loaded from off-chip memory is sufficient to support all computations, all logic units can operate in parallel, and no pipelining is required. In the partial pipeline case, the off-chip data loading is insufficient to fully sustain parallel execution, but pipelining allows the available computing resources to be effectively utilized without leaving idle units. In contrast, the full pipeline case occurs when some computing resources remain underutilized even with pipelining across all k clock cycles. A formal definition of these cases is provided in Algorithm 1. As also shown in Fig. 11, these three pipeline strategies are illustrated for different on-chip resource

Algorithm 1 Pipeline Strategy.

Input: A layer \mathcal{L} of convolutional neural network.

Output: A strategy for resource allocation and data processing.

```

1:  $n_{onchip}$ : neurons on chip for current layer
2:  $n_{memcover}$ : neurons covered under memory load capability
3:  $D_{layer}$ : current layer's delay
4:  $\tau$ : system clock period
5:  $k$ : stochastic bitstream length
6: if  $n_{onchip} < n_{memcover}$  then
7:   no pipeline,  $n_{parallel} = n_{onchip}$ 
8:    $D_{layer} = cycle_{unpipe} \times k \times \tau$ 
9: else
10:  pipeline can be used,  $n_{parallel} < n_{onchip}$ 
11:   $incycle_{pipe} = ceil(n_{onchip}/n_{memcover})$ 
12:  if  $incycle_{pipe} < k$  then
13:    partial pipeline
14:     $D_{layer} = [cycle_{pipe}(k + 1) + incycle_{pipe} - 1] \times \tau$ 
15:  else
16:    full pipeline
17:     $D_{layer} = (k + incycle_{pipe}) \times \tau$ 
18:  end if
19: end if

```

availability and memory bandwidth constraints.

V. SIMULATION RESULTS

This section will discuss the simulation results of the proposed SCNN accelerators based on different technologies. We focus on exploring the potential of RFETs in stochastic computing, with FinFETs serving as the reference counterpart for comparison. System-level simulations are performed using the Cadence Genus EDA tool with suitable constraints, based on the open-source 10nm three-independent-gate 4-nanowire RFET standard cell library developed by Gauchi et al [39]. Since no corresponding open-source 10nm FinFET library is available, we adopt the widely used ASAP 7nm library and scale it to the equivalent 10nm node [40]. The scaling method used here is supported by [41, 42]. To ensure a fair comparison, both RFET and FinFET use the same logic gate library with minimum drive strength. For the RFET-based accelerator, the memory components still use FinFETs, and all other modules are based on the proposed design using RFET technology. The supply voltage for the RFET system is 0.85V, which provides a balance between speed and energy efficiency, whereas the

TABLE I

ACCURACY, AREA, DELAY, AND ENERGY COMPARISON BETWEEN FINFET- AND RFET-BASED 8-BIT PCC AND 32-BIT APCS

	8-bit PCC			Traditional APC			Reference AxPC			Proposed MAJ-AxPC			Proposed COMP-AxPC		
MSE/MAE	NA			As the baseline			0.0059/0.059 (medium)			0.0067/0.064 (high)			0.0051/0.054 (low)		
Technology	Area (μm^2)	Delay (ps)	Energy (fJ)	Area (μm^2)	Delay (ps)	Energy (fJ)	Area (μm^2)	Delay (ps)	Energy (fJ)	Area (μm^2)	Delay (ps)	Energy (fJ)	Area (μm^2)	Delay (ps)	Energy (fJ)
FinFET10nm	2.2	242	4.1	32.1	352	87.6	10.7	189	21.8	7.3	166	19.3	13.8	269	33.5
RFET10nm	2.0	142	2.9	26.2	334	54.6	9.1	124	16.1	6.0	151	12.0	12.1	171	20.9
Gain to FinFET	9.1%	41.3%	29.3%	18.4%	5.7%	37.7%	15.0%	34.4%	26.1%	17.8%	9.0%	37.8%	12.3%	36.4%	37.6%

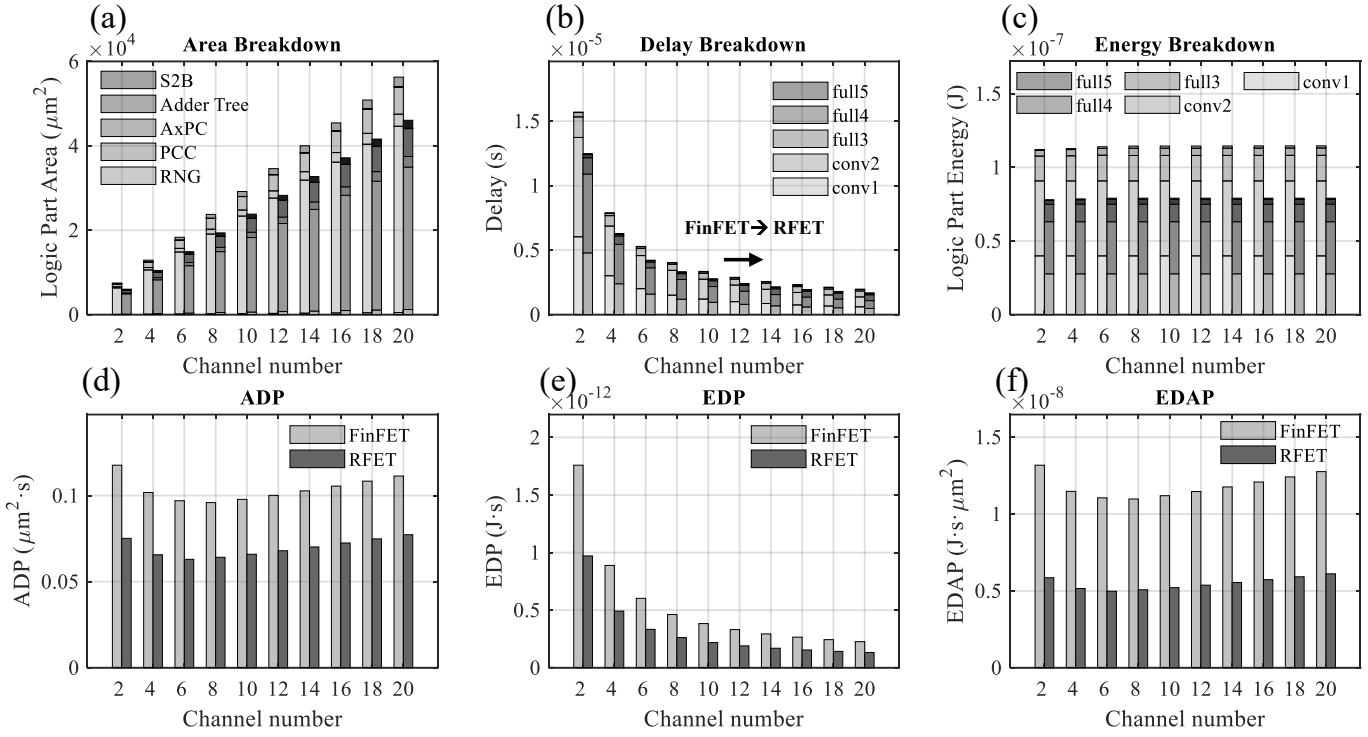


Fig. 12. System-level performance comparison between FinFET- and RFET-based SCNNs. Left bars represent FinFET, right bars represent RFET.

TABLE II
CHANNEL-LEVEL AREA, DELAY, AND ENERGY COMPARISON

Parameters	FinFET	RFET	Gain
Channel Area (μm^2)	2710	2223	18%
Min Clock Period (ns)	0.82	0.64	22%
Switching Energy (pJ)	4.22	2.94	30%

supply voltage for the FinFET is set to 0.7V as defined in the ASAP 7nm library.

A. Performance Comparison of FinFET and RFET Blocks

As shown in Table I, two key components—an 8-bit PCC and the 25-input COMP-AxPC with 32-bit bitstream—are analyzed in detail under both FinFET and RFET technologies. For the PCC, the RFET-based implementation demonstrates notable improvements in area, delay, and switching energy compared with its FinFET counterpart, achieving reductions of approximately 9%, 41%, and 29%, respectively. The area reduction is primarily attributed to the reduced number of RFET transistors, despite the fact that the footprint of a single RFET is larger than that of its FinFET counterpart. The delay reduction is mainly attributed to the lower internal and load capacitance along the critical path enabled by the more compact RFET logic structure, despite the smaller on-state current compared with FinFET devices. In addition, the reduction in switching energy comes from the significantly lower transistor count of the RFET-based design.

A similar performance trend is observed for the RFET-based APC and AxPCs. In most scenarios, RFETs can

effectively optimize performance compared to FinFETs. The proposed RFET-based MAJ-AxPCs achieve high performance while incurring only a slight loss in accuracy, whereas the COMP-AxPC attains higher accuracy while preserving the performance advantages over traditional FinFET-based APC and AxPC designs. Table II compares FinFET and RFET implementations in terms of area, clock period, and energy per channel. The RFET implementation achieves an 18% reduction in channel area, a 22% improvement in clock period, and a 30% decrease in switching energy, clearly demonstrating its advantages over FinFET technology. Besides, recent advancements aimed at improving the on-state current of RFETs are expected to further mitigate current limitations and strengthen the overall advantages of RFET-based designs [42-44].

B. System-level Simulation Results

The system-level simulation is conducted to identify the optimal channel number and to compare the performance of FinFET-based and RFET-based accelerators. As shown in Fig. 12, the logic part area of the system increases linearly with the number of channels, while the latency decreases as the channel count grows. The area breakdown indicates that the primary contributor to the overall area is the PCC, with the AxPC and adder tree also contributing significantly. With more channels, additional resources are available for parallel processing; however, the delay eventually approaches a limit imposed by memory bandwidth. Most of the latency originates from the convolutional layers, which involve a large number of neurons. The energy consumption of the logic part remains relatively

TABLE III
COMPARISON WITH OTHER STATE-OF-THE-ART ACCELERATOR WORKS

	ISSCC 21 [43]	TCAD 18 [6]	TCASII 22 [44]	SSCL 22 [37]	TNNLS 23 [35]	This Work	
NN Type	Digital	SC	SC	SC	SC	SC	
Technology	CMOS	CMOS	CMOS	CMOS	CMOS	CMOS	RFET
Tech Node	7nm	45nm	65nm	14nm	40nm	10nm	10nm
Voltage	0.55-0.75V	Not Applied	1.0V	0.6-0.9V	Not Applied	0.7V	0.85V
Clock	1.0-1.6GHz	481MHz	909MHz	250-500MHz	200 MHz	1.25GHz	1.57GHz
Precision	FP8-32	7	5	4-8	8	8	8
Area	19.6 μm^2	22.9 μm^2	0.006 μm^2	0.5 μm^2	2.1 μm^2	0.237 μm^2	0.194 μm^2
Power	Not Applied	2600mW	4.06mW	16-68mW	651mW	13.9mW	12.2mW
TOPS/W	8.9-16.5	5.66	2.17	4.4-75	0.34	12.12	16.82
TOPS/mm²	3.27-5.22	0.64	1.44	0.3-4.8	0.11	7.09	10.60
MNIST Accuracy	Not Applied	99.07%	98.8%	95.1%-98.7%	97.6%	98.5%	
CIFAR10 Accuracy	Not Applied	Not Applied	Not Applied	69.4%-71.7%	81%	73.1%	

unchanged, as the majority of the energy arises from switching activity, and the total switching-induced energy remains constant.

To determine an appropriate channel number, three commonly used system-level metrics—area-delay product (ADP), energy-delay product (EDP), and energy-delay-area product (EDAP)—are employed as evaluation criteria. Based on the plots of ADP and EDAP, the optimal channel number is found to be 8 for both FinFET and RFET technologies. At this configuration, the RFET-based accelerator achieves reductions of up to 18% in area, 18% in delay, and 31% in energy, resulting in an overall EDAP improvement of 54%.

To determine the optimal bitstream length for the SCNN system, training is performed using PyTorch. However, since PyTorch does not natively support all the mathematical functions required for SCNNs, the training process relies on the insertion of equivalent SC models. Specifically, the mathematical model of SC is encapsulated as a Python function and integrated into the training pipeline. The inference flow is constructed in the same manner, strictly adhering to the adopted SCNN structure.

Two commonly used CNN datasets, MNIST and CIFAR-10, are employed for evaluation. The MNIST is based on the LeNet-5 CNN structure, while the CIFAR-10 follows the same network structure as the reference work [45]. Overall, the model accuracy increases with both the bitstream length and the system precision. The system precision defines the accuracy ceiling; higher precision leads to a higher upper limit, although the improvement becomes negligible once the precision exceeds five bits. With respect to bitstream length, accuracy improves rapidly when the length is small, but the rate of improvement slows down as the length increases, eventually reaching a stable level. Based on the simulation results, the SCNN model achieves accuracies of up to 98.5% on MNIST and 73.1% on CIFAR-10.

C. Comparison with State-of-the-Art Works

Table III provides a comparative overview of several recent works on SCNN and digital neural network accelerators

[6, 36, 43, 44]. The design presented in this work employs RFET-based technology at the 10nm node, and the SCNN operates with 8-bit system precision and uses 32-bit bitstream length with unipolar encoding. Operating at 0.85V with a maximum clock frequency of 1.57GHz, the design maintains competitive performance among SC implementations. It also features a compact area footprint of 0.194mm², including 10KB on-chip memory, which is smaller than that of designs such as SSCL 22 (0.5mm²) and TNNLS 23 (2.1mm²). The simulated power consumption is at 19mW, contributing to an energy efficiency of 16.82 TOPS/W, which compares favorably with several prior works. Additionally, a computational density of 10.6 TOPS/mm² is achieved. In terms of inference accuracy, the design attains 98.5% on the MNIST and 73.1% on the CIFAR-10 datasets, demonstrating reasonable performance for SC-based approaches. To improve TOPS/W, shorter bitstreams such as 16-bit or even 8-bit representations can be used. However, this comes at the cost of reduced numerical precision and degraded model accuracy. Overall, the results suggest that the use of RFET technology provides great benefits in balancing power, performance, and area in stochastic neural network accelerators.

VI. CONCLUSIONS

In this paper, a compact and efficient RFET-based SCNN accelerator is proposed, featuring optimized key components, such as PCCs and APCs. Leveraging the reconfigurable properties of RFETs, we demonstrate—through both mathematical analysis and simulation—that PCCs can be designed with significantly reduced area. System-level simulations based on a widely adopted accelerator architecture indicate that, under the same technology node, the RFET-based SCNN achieves up to 18% area reduction, 18% latency improvement, and 31% switching energy savings under 8-bit accuracy and 32-bit bitstream compared to the FinFET counterpart. These enhancements lead to an overall improvement of 39% in TOPS/W and 49% in TOPS/mm².

ENERGY-EFFICIENT RFET-BASED STOCHASTIC COMPUTING NN ACCELERATOR

REFERENCES

- [1] N. K. Upadhyay *et al.*, "Emerging memory devices for neuromorphic computing," *Advanced Materials Technologies*, vol. 4, no. 4, p. 1800589, 2019.
- [2] O. I. Abiodun *et al.*, "State-of-the-art in artificial neural network applications: A survey," *Heliyon*, vol. 4, no. 11, 2018.
- [3] Y. Liu *et al.*, "A survey of stochastic computing neural networks for machine learning applications," *IEEE Transactions on Neural Networks and Learning Systems*, vol. 32, no. 7, pp. 2809-2824, 2020.
- [4] A. Ardakani *et al.*, "VLSI implementation of deep neural network using integral stochastic computing," *IEEE Transactions on Very Large Scale Integration (VLSI) Systems*, vol. 25, no. 10, pp. 2688-2699, 2017.
- [5] A. Ren *et al.*, "Se-denn: Highly-scalable deep convolutional neural network using stochastic computing," *ACM Sigplan Notices*, vol. 52, no. 4, pp. 405-418, 2017.
- [6] Z. Li *et al.*, "HEIF: Highly efficient stochastic computing-based inference framework for deep neural networks," *IEEE Transactions on Computer-Aided Design of Integrated Circuits and Systems*, vol. 38, no. 8, pp. 1543-1556, 2018.
- [7] K. Kim *et al.*, "An energy-efficient random number generator for stochastic circuits," in *2016 21st Asia and South Pacific Design Automation Conference (ASP-DAC)*, 2016: IEEE, pp. 256-261.
- [8] K. Zhong *et al.*, "A Brief Survey on Randomizer Design and Optimization for Efficient Stochastic Computing," in *2024 IEEE International Test Conference in Asia (ITC-Asia)*, 2024: IEEE, pp. 1-6.
- [9] K. Zhong *et al.*, "Towards low-cost high-accuracy stochastic computing architecture for univariate functions: design and design space exploration," in *2022 Design, Automation & Test in Europe Conference & Exhibition (DATE)*, 2022: IEEE, pp. 346-351.
- [10] Y. Ding *et al.*, "Generating multiple correlated probabilities for MUX-based stochastic computing architecture," in *2014 IEEE/ACM International Conference on Computer-Aided Design (ICCAD)*, 2014: IEEE, pp. 519-526.
- [11] C. Collinsworth *et al.*, "Stochastic number generators with minimum probability conversion circuits," in *2021 IEEE Computer Society Annual Symposium on VLSI (ISVLSI)*, 2021: IEEE, pp. 49-54.
- [12] K. Kim *et al.*, "Approximate de-randomizer for stochastic circuits," in *2015 International SoC Design Conference (ISOCC)*, 2015: IEEE, pp. 123-124.
- [13] C. Pan *et al.*, "A proposal for energy-efficient cellular neural network based on spintronic devices," *IEEE Transactions on Nanotechnology*, vol. 15, no. 5, pp. 820-827, 2016.
- [14] M. W. Daniels *et al.*, "Energy-efficient stochastic computing with superparamagnetic tunnel junctions," *Physical review applied*, vol. 13, no. 3, p. 034016, 2020.
- [15] C. Pan *et al.*, "An expanded benchmarking of beyond-CMOS devices based on Boolean and neuromorphic representative circuits," *IEEE Journal on Exploratory Solid-State Computational Devices and Circuits*, vol. 3, pp. 101-110, 2018.
- [16] N. Kavand *et al.*, "Design of energy-efficient RFET-based exact and approximate 4: 2 compressors and multipliers," *IEEE Transactions on Circuits and Systems II: Express Briefs*, vol. 70, no. 9, pp. 3644-3648, 2023.
- [17] A. Heinzig *et al.*, "Reconfigurable silicon nanowire transistors," *Nano letters*, vol. 12, no. 1, pp. 119-124, 2012.
- [18] M. Reuter *et al.*, "From mosfets to ambipolar transistors: Standard cell synthesis for the planar rfet technology," *IEEE Transactions on Circuits and Systems I: Regular Papers*, vol. 68, no. 1, pp. 114-125, 2020.
- [19] T. Mikolajick *et al.*, "Reconfigurable field effect transistors: A technology enablers perspective," *Solid-State Electronics*, vol. 194, p. 108381, 2022.
- [20] T. Mikolajick *et al.*, "The RFET—A reconfigurable nanowire transistor and its application to novel electronic circuits and systems," *Semiconductor Science and Technology*, vol. 32, no. 4, p. 043001, 2017.
- [21] S. Rai *et al.*, "Designing efficient circuits based on runtime-reconfigurable field-effect transistors," *IEEE Transactions on Very Large Scale Integration (VLSI) Systems*, vol. 27, no. 3, pp. 560-572, 2018.
- [22] J. Romero-González *et al.*, "An efficient adder architecture with three-independent-gate field-effect transistors," in *2018 IEEE International Conference on Rebooting Computing (ICRC)*, 2018: IEEE, pp. 1-8.
- [23] J. Trommer *et al.*, "Functionality-enhanced logic gate design enabled by symmetrical reconfigurable silicon nanowire transistors," *IEEE Transactions on Nanotechnology*, vol. 14, no. 4, pp. 689-698, 2015.
- [24] S. Lu *et al.*, "A Novel RFET-Based FPGA Architecture Based on Delay-Aware Packing Algorithm," *IEEE Transactions on Emerging Topics in Computing*, 2025.
- [25] S. Lu *et al.*, "Technology/System Co-Optimization for FPGA Using Emerging Reconfigurable Logic Device," *ACM Journal on Emerging Technologies in Computing Systems*, vol. 21, no. 3, pp. 1-21, 2025.
- [26] R. Saravanan *et al.*, "Reconfigurable fet approximate computing-based accelerator for deep learning applications," in *2023 IEEE International Symposium on Circuits and Systems (ISCAS)*, 2023: IEEE, pp. 1-5.
- [27] J. Zhang *et al.*, "Configurable circuits featuring dual-threshold-voltage design with three-independent-gate silicon nanowire FETs," *IEEE Transactions on Circuits and Systems I: Regular Papers*, vol. 61, no. 10, pp. 2851-2861, 2014.
- [28] M. Simon *et al.*, "A wired-AND transistor: Polarity controllable FET with multiple inputs," in *2018 76th Device Research Conference (DRC)*, 2018: IEEE, pp. 1-2.
- [29] J. Trommer *et al.*, "Enabling energy efficiency and polarity control in germanium nanowire transistors by individually gated nanojunctions," *ACS nano*, vol. 11, no. 2, pp. 1704-1711, 2017.
- [30] J. Zhang *et al.*, "Polarity-controllable silicon nanowire transistors with dual threshold voltages," *IEEE Transactions on Electron Devices*, vol. 61, no. 11, pp. 3654-3660, 2014.
- [31] J.-H. Bae *et al.*, "Reconfigurable field-effect transistor as a synaptic device for XNOR binary neural network," *IEEE Electron Device Letters*, vol. 40, no. 4, pp. 624-627, 2019.
- [32] A. Alaghi *et al.*, "The promise and challenge of stochastic computing," *IEEE Transactions on Computer-Aided Design of Integrated Circuits and Systems*, vol. 37, no. 8, pp. 1515-1531, 2017.
- [33] P. Purwono *et al.*, "Understanding of convolutional neural network (cnn): A review," *International Journal of Robotics and Control Systems*, vol. 2, no. 4, pp. 739-748, 2022.
- [34] D. Ghimire *et al.*, "A survey on efficient convolutional neural networks and hardware acceleration," *Electronics*, vol. 11, no. 6, p. 945, 2022.
- [35] C. F. Frasser *et al.*, "Fully parallel stochastic computing hardware implementation of convolutional neural networks for edge computing applications," *IEEE Transactions on Neural Networks and Learning Systems*, vol. 34, no. 12, pp. 10408-10418, 2022.
- [36] J. Yang *et al.*, "A 65-nm Digital Stochastic Compute-in-Memory CNN Processor With 8-bit Precision," *IEEE Journal of Solid-State Circuits*, 2025.
- [37] W. Romaszkan *et al.*, "A 4.4–75-tops/w 14-nm programmable, performance-and precision-tunable all-digital stochastic computing neural network inference accelerator," *IEEE Solid-State Circuits Letters*, vol. 5, pp. 206-209, 2022.
- [38] H. Xiong *et al.*, "Hardware implementation of an improved stochastic computing based deep neural network using short sequence length," *IEEE Transactions on Circuits and Systems II: Express Briefs*, vol. 67, no. 11, pp. 2667-2671, 2020.
- [39] R. Gauchi *et al.*, "An open-source three-independent-gate fet standard cell library for mixed logic synthesis," in *2022 IEEE International Symposium on Circuits and Systems (ISCAS)*, 2022: IEEE, pp. 273-277.
- [40] L. T. Clark *et al.*, "ASAP7: A 7-nm finFET predictive process design kit," *Microelectronics Journal*, vol. 53, pp. 105-115, 2016.
- [41] "International Roadmap for Devices and Systems (IRDSTM) 2017 Edition." IEEE. <https://irds.ieee.org/editions/2017> (accessed October 5, 2025).
- [42] M. N. A. Taj, *Intel Chip Manufacturing Technology Roadmap*, 2022.
- [43] A. Agrawal *et al.*, "9.1 A 7nm 4-core AI chip with 25.6 TFLOPS hybrid FP8 training, 102.4 TOPS INT4 inference and workload-aware throttling," in *2021 IEEE International Solid-State Circuits Conference (ISSCC)*, 2021, vol. 64: IEEE, pp. 144-146.
- [44] H. Wang *et al.*, "An efficient stochastic convolution architecture based on fast FIR algorithm," *IEEE Transactions on Circuits and Systems II: Express Briefs*, vol. 69, no. 3, pp. 984-988, 2021.